CRACK INITIATION CRITERIA FOR DEFORMED ANISOTROPIC R260 RAIL STEEL

12th International Conference on Contact Mechanics and Wear of Rail/Wheel Systems (CM2022), Melbourne, Australia, 4-7 September 2022

CRACK INITIATION CRITERIA FOR DEFORMED ANISOTROPIC R260 RAIL STEEL

Nasrin Talebi[1,*], Johan Ahlström[2], Magnus Ekh[1], Knut Andreas Meyer[3]

[1]Department of Industrial and Materials Science, Division of Material and Computational Mechanics/ CHARMEC
[2]Department of Industrial and Materials Science, Division of Engineering Materials/CHARMEC
Chalmers University of Technology, SE-412 96 Gothenburg, Sweden
[3]Institute of Applied Mechanics, TU Braunschweig, DE-38106, Braunschweig, Germany

*E-mail: nasrint@chalmers.se

Abstract: Rail material selection and maintenance planning require accurate material failure criteria. While many of these criteria consider low-cycle fatigue of virgin materials, rail failure is known to occur after severe plastic deformations. It is, therefore, relevant to consider the applicability of such criteria during large plastic deformations. In this study, we simulate previously performed high-shear tension-torsion experiments using finite strain theory to evaluate the local stresses and strains. Based on these results, failure criteria are calibrated and validated. The Jiang-Sehitoglu criterion accurately fits and predicts failure. However, the identified parameter values are different from literature values for similar materials.

Keywords: Anisotropy; Tension-torsion; Plasticity; FE simulations; Crack initiation criteria.

1. Introduction

Rolling Contact Fatigue (RCF) crack initiation is often connected to the accumulation of plastic deformation in the surface layer of rails and wheels. The behavior and strength of this highly deformed and anisotropic layer are thus key properties of a rail or wheel material. These properties also change with traffic since both the depth and degree of anisotropy evolve. Establishing crack initiation models that are experimentally validated is of great importance in railway engineering to increase reliability in maintenance action planning and actions to improve traffic safety.

A great challenge is to measure these properties. Examples of contributions in literature are Wetscher et al. [1], Hohenwarter et al. [2], and Meyer et al. [3]. In [1], an equal channel angular pressing technique, while in [2], a high-pressure torsion technique was used to determine the properties of rail steel R260. In [3], an axial-torsion machine was used to apply an axial loading combined with large shear deformations to R260 steel. It was found that the deformed steel in the specimens had similar properties to those found in the anisotropic surface layer of field samples. An advantage of this technique is that cyclic loading can be combined with large shear deformations. In this contribution, we use experimental results from this technique to evaluate different crack initiation criteria.

Various failure initiation criteria for rolling-contact situations have been proposed in the literature, see, e.g. the review by Sadeghi et al. [4]. One criterion was formulated by Kapoor [5], where the von Mises equivalent ratcheting strain in each loading cycle contributes to the damage evolution. Others use the critical plane approach, such as in Dang Van et al. [6]. In Jiang and Sehitoglu [7], a criterion combining fatigue damage (by using critical plane search approach) and ratcheting damage is proposed. As compared to the criteria by Dang Van et al. [6] and Jiang and Sehitoglu [7], the Kapoor [5] criterion does not account for a dependence on the hydrostatic stress or strain. The benefit of the Kapoor criterion is that no search for a critical plane is needed. However, a limitation of the above-mentioned criteria is that they do not account for the microstructure, which is very important for rolling contact fatigue as pointed out by e.g. Alley and Neu [8]. A crack initiation model accounting for the highly deformed surface layer in rails is presented in Trummer et al. [9].

In this contribution, we model the cyclic plasticity behavior during the tension-torsion tests by using a material model proposed in Meyer et al. [10] in a finite element model of the specimens. By using the obtained stress and strain histories, the failure initiation criteria by Kapoor [5] and Jiang and Sehitoglu [7] are applied and evaluated against experimental data.

2. Experiments

A method for predeforming test bars to replicate the large shear strains in the surface layer of rails has been developed by Meyer et al. [3]. The predeformation method starts by extracting pearlitic R260 steel test bars from virgin railheads along the rolling direction. The bars are subjected to axial and torsional loading in an axial-torsion

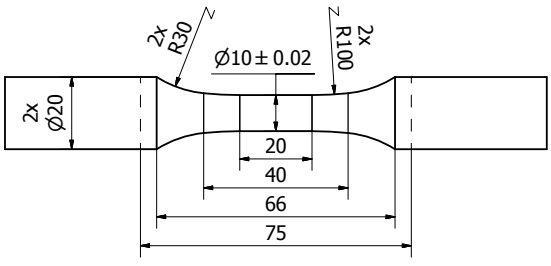

Figure 1: *Test bar dimensions in mm*

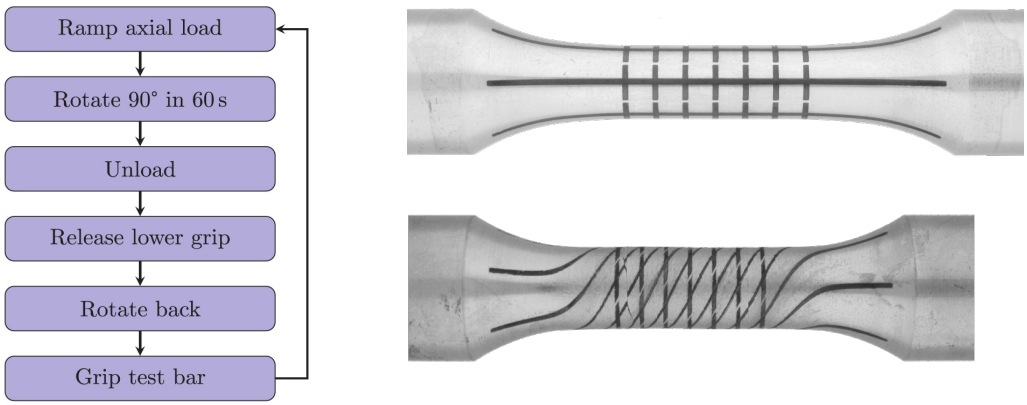

Figure 2: *The predeformation procedure (left), undeformed test bar (top right), and deformed test bar (bottom right).*

machine to achieve similar loading conditions to those in the surface layer of in-service rails (i.e., high shear as well as compressive stresses). The test bars have a $10\,\mathrm{mm}$ gauge diameter and a $20\,\mathrm{mm}$ gauge length, see Fig. 1. Each bar is twisted in steps of 90 degrees under a constant axial load; the full procedure is illustrated in Fig. 2 (left), and a test bar before and after deformation is shown in Fig. 2 (right). By comparing the marks on the undeformed and deformed bars, the surface shear strain can be measured. The specimens are subjected to different nominal axial stresses: -500, -250, 0 and 250 MPa. The resulting torque versus twist for the different axial stresses are shown in Fig. 4a. From these results, we can observe that the torsional stiffness has been increased for compressive loadings due to an increase in the gauge diameter of the specimens. To avoid buckling during twisting, the amount of compressive stress was limited to 500 MPa. Meyer et al. [11] found no significant change of elastic parameters due to predeformation (i.e. less than 4% change in the shear modulus after the maximum predeformation), motivating the use of models where damage is decoupled from a plasticity model. Thereby, the damage predictions will be implemented as a post-processing step to the FE modeling in this study. Another important observation according to Fig. 4a is a significant influence of axial load on the amount of twist a specimen can withstand before failure. It is known that rolling contact loading is a combination of compressive and shear stresses ([7], [12]), which motivates studying the fatigue behavior of the predeformed test bars as the main focus of this paper. It should be mentioned that failure is defined by the torque dropping $2\,\mathrm{Nm}$ below the maximum previously measured value, and all the test bars had visible cracks at this point.

3. Modeling of predeformation tests

Stress and strain histories are required to evaluate different crack initiation criteria, but Meyer et al. [10] only measured the specimen's elongation, axial force, twist, and torque. We obtain the local stresses and strains from an axisymmetric finite element model (cf. [10]). The present section introduces the finite element simulation and the material model before analyzing the stress and strain responses.

3.1. Finite element model

The finite element analysis is performed in the commercial FE code Abaqus [13] using 8-node axisymmetric elements with additional twist degrees of freedom. This means that the element discretization is in the 2D axisymmetric plane but the degrees of freedom in the nodes are displacements in the radial $u_r(r,z)$ and z-direction $u_z(r,z)$ as well as twist $\varphi(r,z)$, see Figure 3.

3.2. Material model

The accuracy of the FE-modeling relies on an accurate description of the material behavior. We, therefore, adopt the finite strain "BC2" model formulation and calibration from Meyer et al. [10]. A summary of the model and its parameters is given here for completeness.

The model is based on the multiplicative split of the deformation gradient, $\boldsymbol{F} = \boldsymbol{F}_\mathrm{e}\boldsymbol{F}_\mathrm{p}$, and the compressible isotropic Neo-Hookean hyperelastic free energy

$$\Psi(\boldsymbol{x}) = \frac{k_1}{2}\mathrm{tr}\left(\frac{\boldsymbol{x}}{\sqrt[3]{I_{3x}}} - \boldsymbol{I}\right) + \frac{k_2}{2}\left[\sqrt{I_{3x}} - 1\right]^2 \quad (1)$$

where the third invariant $I_{3x} = \det(\boldsymbol{x})$. The Mandel stress, $\boldsymbol{M}$, and the back-stresses, $\boldsymbol{M}_{\mathrm{k},i}$, are then given by

$$\boldsymbol{M} = 2\boldsymbol{C}_\mathrm{e}\frac{\partial\Psi_\mathrm{e}(\boldsymbol{C}_\mathrm{e})}{\partial\boldsymbol{C}_\mathrm{e}}, \quad k_1 = G,\, k_2 = K \quad (2)$$

$$\boldsymbol{M}_{\mathrm{k},i} = 2\boldsymbol{c}_{\mathrm{k},i}\frac{\partial\Psi_{\mathrm{k},i}(\boldsymbol{c}_{\mathrm{k},i})}{\partial\boldsymbol{c}_{\mathrm{k},i}}, \quad k_1 = H_{\mathrm{k},i},\, k_2 = 0 \quad (3)$$

where G and K are the elastic shear and bulk moduli, and $H_{\mathrm{k},i}$ are the kinematic hardening moduli. $\boldsymbol{C}_\mathrm{e} = \boldsymbol{F}_\mathrm{e}^\mathrm{T}\boldsymbol{F}_\mathrm{e}$ is the standard elastic right Cauchy-Green deformation tensor. By introducing deformation gradients associated

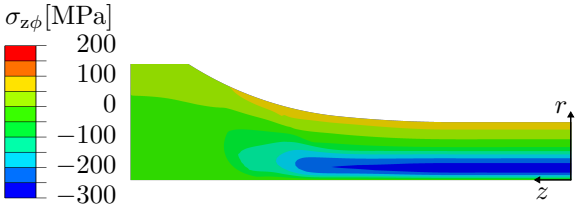

Figure 3: *Residual stresses after 8 cycles at $-500\,\mathrm{MPa}$ (adapted from [10]), showing the modeling domain and coordinate system.*

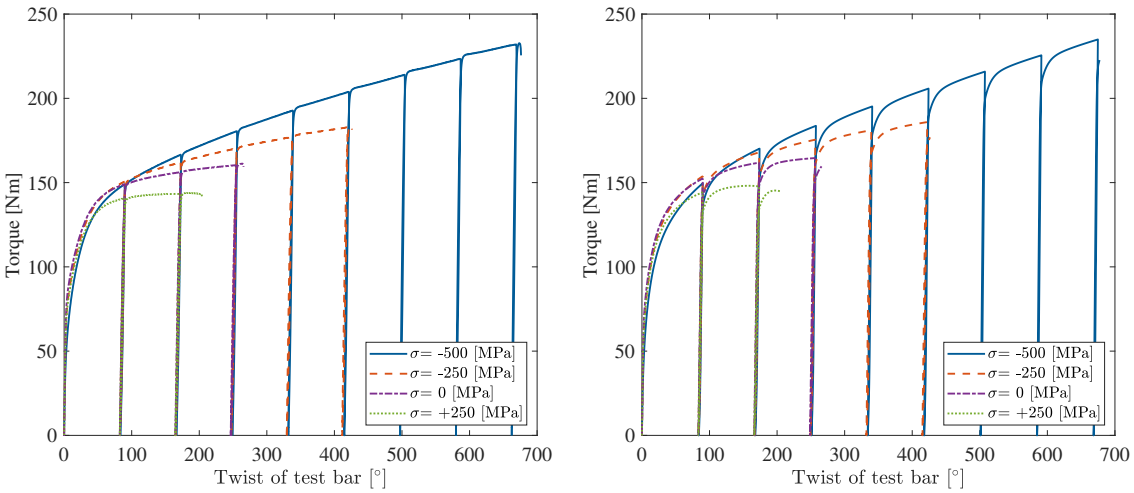

(a) *Experimental results* **(b)** *Simulation results*

Figure 4: *Torque responses for different nominal axial stresses*

with the kinematic hardening, $\boldsymbol{F}_{\mathrm{k},i}$, the deformation tensors $\boldsymbol{c}_{\mathrm{k},i} = \boldsymbol{F}_{\mathrm{k},i}^{-T}\boldsymbol{F}_{\mathrm{k},i}^{-1}$ are introduced. The stresses $\boldsymbol{M}$ and $\boldsymbol{M}_{\mathrm{k},i}$ are used with a von Mises yield criterion,

$$\Phi = \sqrt{\frac{3}{2}}\left|\boldsymbol{M}^{\mathrm{dev}} - \sum_{i=1}^{2}\boldsymbol{M}_{\mathrm{k},i}^{\mathrm{dev}}\right| - [Y_0 + \kappa] \qquad (4)$$

where Y_0 is the initial yield limit and κ is the isotropic hardening stress. The model adopts associative evolution of the plastic deformation gradient,

$$\dot{\boldsymbol{F}}_{\mathrm{p}}\boldsymbol{F}_{\mathrm{p}}^{-1} = \boldsymbol{L}_{\mathrm{p}} = \dot{\lambda}\frac{\partial\Phi}{\partial\boldsymbol{M}} = \dot{\lambda}\boldsymbol{\nu} \qquad (5)$$

with the plastic multiplier $\dot{\lambda}$. The nonlinear Voce-type isotropic hardening,

$$\dot{\kappa} = \dot{\lambda}H_{\mathrm{iso}}\left[1 - \frac{\kappa}{\kappa_\infty}\right] \qquad (6)$$

is adopted, introducing the isotropic hardening modulus H_{iso} and saturation stress κ_∞. The nonlinear kinematic hardening,

$$\boldsymbol{L}_{\mathrm{k},i} = \dot{\lambda}\left[-\boldsymbol{\nu} + \delta\frac{3}{2}\frac{\boldsymbol{M}_{\mathrm{k},i}^{\mathrm{T}}}{Y_{\mathrm{k},i}} + [1-\delta]\frac{\boldsymbol{M}_{\mathrm{k},i} : \boldsymbol{\nu}}{Y_{\mathrm{k},i}}\boldsymbol{\nu}\right] \qquad (7)$$

where $\boldsymbol{L}_{\mathrm{k},i} = \dot{\boldsymbol{F}}_{\mathrm{k},i}\boldsymbol{F}_{\mathrm{k},i}^{-1}$, ensures accurate results for the non-proportional loading. The parameter $Y_{\mathrm{k},i}$ controls the saturation of the ith back-stress, $\boldsymbol{M}_{\mathrm{k},i}$, and δ controls the relation between the Armstrong-Frederick and Burlet-Cailletaud type of kinematic hardening.

The values of the elastic parameters, shear modulus $G = 80.5\,\mathrm{GPa}$ and Young's modulus $E = 212\,\mathrm{GPa}$, were obtained directly from the experiments in [10] ($K = EG/[9G - 3E]$). The remaining parameter values, given in Table 1, were obtained from a calibration procedure.

The open-source implementation [14] of the material model as a user subroutine (UMAT) for Abaqus has been used. It adopts the implicit backward Euler time discretization scheme. As pointed out in Section 2, the damage evolution is uncoupled from the mechanical behavior in this paper.

Table 1: *Material parameters for the plastic behavior of the model.*

Y_0	δ	H_{iso}	κ_∞	$H_{\mathrm{k},1}$	$Y_{\mathrm{k},1}$	$H_{\mathrm{k},2}$	$Y_{\mathrm{k},2}$
451	0.290	212	169	1450	293	10.148	322
MPa	-	MPa	MPa	MPa	MPa	MPa	MPa

3.3. Modeling results

Fig. 4b shows the simulated torque versus twist for different axial loads. While the model accurately describes the torque magnitude in each cycle, it predicts a smoother elastic to plastic transition than what is observed in the experiments. As noted in [10], the high strain rate and a slight material rate dependence can partly explain this effect. Furthermore, the peak torque in each cycle is slightly overpredicted. As previously shown, the magnitude of the axial displacement is also accurately predicted by the model [10]. Overall, the model predictions are considered sufficiently accurate for evaluating fatigue criteria.

In Fig. 5, the time histories of the Cauchy stresses and the logarithmic strains are shown. The evaluation point is close to the surface and in the middle of the gauge length of the specimens. In all cases, the local axial Cauchy stress, σ_{zz}, is approximately equal to the applied nominal stress after the first axial load application ($t = 3\,\mathrm{s}$). The magnitude of the axial stress component close to the surface decreases during the torsion loading. This effect is caused by the higher shear stresses at the surface, causing the center of the bar to take a higher portion of the axial stress. Due to residual stresses caused by these stress gradients, both the axial and shear stress change sign during unloading.

Tensile axial loads reduce the gauge diameter resulting in the localization of shear strains in the center of the gauge length. For compressive loads, the shear strains remain constant over a longer distance. In Fig. 5b, this effect

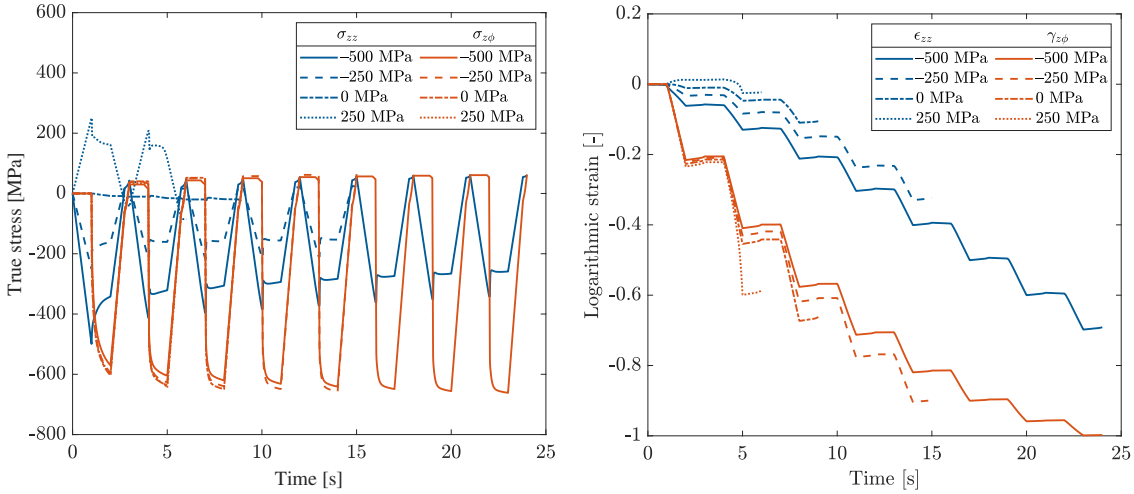

(a) *Cauchy stresses* **(b)** *Logarithmic strains*

Figure 5: *Simulated stress and strain times histories for each axial load at* $z = 0.40\,\mathrm{mm}$ *and* $r = 4.7\,\mathrm{mm}$

causes the shear strain ratcheting increment to be higher for tensile axial loads than for compressive axial loads. We note that the axial strain, ϵ_{zz}, becomes negative also for tensile axial loading due to the shear-induced rotations. This effect is due to the definition of the logarithmic strain on the deformed configuration (see [13]).

4. Crack initiation criteria

Different crack initiation criteria can be evaluated based on the simulated stress-strain histories in Section 3. Jiang and Sehitoglu [7] (J-S criterion) have proposed a critical plane based low cycle fatigue criterion. For a given plane defined by the normal $\boldsymbol{n}$, a fatigue parameter FP is given with a normal and a shear contribution

$$FP = \frac{\Delta\epsilon}{2}\,\sigma_{\max} + J\,\Delta\gamma\,\Delta\tau \tag{8}$$

where $\Delta\epsilon$ is the normal strain range, $\sigma_{\max}$ the maximum normal stress, $\Delta\gamma$ the shear strain range, $\Delta\tau$ the shear stress range during a loading cycle. Furthermore, J is the material parameter which defines the importance of the shear contribution to FP. Note that for brevity of presentation, from hereafter, stress refers to the Cauchy stress and strain refers to the logarithmic strains on the current configuration. The J-S criterion is based on critical plane search (CPS), which surveys all possible planes (defined by the normal $\boldsymbol{n}$) passing through a certain material point in order to seek for the plane with the maximum fatigue parameter, i.e. $\max_{\boldsymbol{n}} FP$. At a given material point, any arbitrary plane can be defined by expressing the normal $\boldsymbol{n}$ in terms of the polar angle $\theta \in [0,\, \pi/2]$ and the azimuthal angle $\phi \in [0,\, 2\,\pi]$. By collecting the Cartesian components of $\boldsymbol{n}$ in a column matrix $\underline{n}$ we have

$$\underline{n} = \begin{bmatrix} \sin(\theta)\,\cos(\phi) \\ \sin(\theta)\,\sin(\phi) \\ \cos(\theta) \end{bmatrix} \tag{9}$$

Stress and strain vectors on a certain plane are obtained by using the normal vector $\boldsymbol{n}$

$$\boldsymbol{t} = \boldsymbol{\sigma}\cdot\boldsymbol{n}, \quad \boldsymbol{t}_\epsilon = \boldsymbol{\epsilon}\cdot\boldsymbol{n} \tag{10}$$

where $\boldsymbol{\sigma}$ and $\boldsymbol{\epsilon}$ are the stress and strain tensor, respectively. The normal stress σ and the normal strain ϵ can then be expressed as

$$\sigma = \boldsymbol{t}\cdot\boldsymbol{n}, \quad \epsilon = \boldsymbol{t}_\epsilon\cdot\boldsymbol{n} \tag{11}$$

The shear stress $\boldsymbol{\tau}$ and the shear strain $\boldsymbol{\gamma}$ are given by

$$\boldsymbol{\tau} = \boldsymbol{t} - \sigma\,\boldsymbol{n}, \quad \boldsymbol{\gamma} = 2\,(\boldsymbol{t}_\epsilon - \epsilon\,\boldsymbol{n}) \tag{12}$$

The normal strain range $\Delta\epsilon$, the shear stress range $\Delta\tau$ and shear strain range $\Delta\gamma$ are computed based on the two time instances in a cycle that gives the largest FP in that particular plane. If the two time instances are t_1 and t_2 then

$$\Delta\epsilon = \epsilon(t_1) - \epsilon(t_2) \tag{13}$$

and

$$\Delta\tau = |\boldsymbol{\tau}(t_1) - \boldsymbol{\tau}(t_2)|\,, \quad \Delta\gamma = |\boldsymbol{\gamma}(t_1) - \boldsymbol{\gamma}(t_2)| \tag{14}$$

Fatigue damage due to Low Cycle Fatigue (LCF) for loading cycle i is denoted $\mathrm{d}D_{\mathrm{f},i}/\mathrm{d}N$ and is calculated as:

$$\frac{\mathrm{d}D_{\mathrm{f},i}}{\mathrm{d}N} = \left(\frac{\langle \max_{\boldsymbol{n}} FP - FP_0\rangle}{C_0}\right)^m \tag{15}$$

where FP_0, m, and C_0 are material parameters which we will determine based on the experimental data in a calibration procedure described in Section 5. Note that we introduced C_0 as a parameter with the same dimension as FP instead of C ($C = C_0^m$) as in [7], whose dimension depends on the exponent m. Furthermore, $\langle\bullet\rangle$ is the Macaulay bracket, which indicates that no fatigue damage would be added from the loading cycle if FP is smaller or equal to FP_0. In this criterion, it is assumed that damage accumulates, and that material failure happens when $D_{\mathrm{f}} = \sum_{i=1}^{N} \mathrm{d}D_{\mathrm{f},i}/\mathrm{d}N = 1$.

Kapoor [5] states that fatigue and ratcheting damage are two competitive failure mechanisms, and the dominant failure mode is the one which gives earlier failure. Ratchetting damage D_r per loading cycle due to the accumulation of plastic strain can according to [5] be expressed

as:

$$\frac{\mathrm{d}D_{\mathrm{r},i}}{\mathrm{d}N} = \frac{1}{\epsilon_c}\frac{\mathrm{d}\epsilon_{\mathrm{vM}}}{\mathrm{d}N} \tag{16}$$

where ϵ_c is the critical strain material parameter, and $\mathrm{d}\epsilon_{\mathrm{vM}}/\mathrm{d}N$ the von Mises effective cycle increment of the strain. It is defined as:

$$\frac{\mathrm{d}\epsilon_{\mathrm{vM}}}{\mathrm{d}N} = \sqrt{\frac{2}{3}}\left|\,\boldsymbol{\epsilon}^{\mathrm{dev}}(t_{\mathrm{end}}) - \boldsymbol{\epsilon}^{\mathrm{dev}}(t_{\mathrm{start}})\right| \tag{17}$$

where $\boldsymbol{\epsilon}^{\mathrm{dev}}(t_{\mathrm{start}})$ and $\boldsymbol{\epsilon}^{\mathrm{dev}}(t_{\mathrm{end}})$ are the deviatoric strain tensors at the beginning and at the end of each loading cycle. In the same way as for the J-S criterion, the damage is accumulated, and when the total ratchetting damage reaches unity, failure happens. It can be noted that this criterion is numerically efficient, since no critical plane search is needed. However, it does not account for the influence of compressive or tensile loading which is observed experimentally, see Section 2.

To account for both ratchetting and fatigue damage, Jiang and Sehitoglu [7] has suggested that material failure happens when the total damage, $D = D_{\mathrm{r}} + D_{\mathrm{f}}$, equals unity:

$$D = \sum_{i=1}^{N}\left(\frac{\mathrm{d}D_{\mathrm{f},i}}{\mathrm{d}N} + \frac{\mathrm{d}D_{\mathrm{r},i}}{\mathrm{d}N}\right) = 1 \tag{18}$$

5. Results

5.1. Material parameter identification

The material parameters for the criteria discussed in Section 4 have been found by using an iterative optimization algorithm. Specifically, the objective function,

$$E_{\mathrm{TOT}} = \frac{1}{\sqrt{N_{\mathrm{p}}}}\sqrt{\sum_{i=1}^{N_{\mathrm{p}}}(N_i^{\mathrm{E}} - N_i^{\mathrm{S}})^2} \tag{19}$$

is minimized. Here, N_i^{E} and N_i^{S} are the number of cycles to failure in experiments and simulations, respectively. The index i denotes each predeformation test and N_{p} the total number of evaluated predeformation tests. According to Fig. 4a, the number of cycles to failure for each predeformation test is not an integer number; for instance, in the case of $\sigma_a = 250$ MPa, material failure happens after cycle 2 and before cycle 3. With this in mind, N_i^{E} is calculated as

$$N_i^{\mathrm{E}} = N + \frac{(\phi_i(t_{\mathrm{end}}) - \phi_i(t_{\mathrm{start}}))_{\mathrm{Last\ cycle}}}{\pi/2} \tag{20}$$

where N is the number of cycles before the failure cycle, and $\phi_i(t_{\mathrm{start}})$ and $\phi_i(t_{\mathrm{end}})$ are twist angles at the beginning and at the end of the last loading cycle (i.e. failure twist angle for predeformation test i) respectively. As mentioned in Section 4, failure is detected when total damage reaches unity. Accordingly, in order to obtain N_i^{S}, a linear interpolation between the cycle number of two subsequent loading cycles (one with lower and one with greater accumulated damage than unity) has been conducted.

The Nelder-Mead simplex algorithm [15] was applied for the optimization. Values from literature for the material parameters FP_0, m, C_0, and ϵ_c have been combined to get different starting guesses for the optimization. The value of J in the J-S criterion is fixed during the optimization to avoid searching for critical planes in each iteration. The FE simulations have been performed for more cycles than those in the experimental tests. However, it may occur that the total damage is less than unity after the simulated number of cycles. In that case, the damage increment in the last cycle is used to extrapolate. If this increment is zero, a large value of N_i^{S} is used to penalize the objective function.

The calibration is only based on the three experiments with axial stresses -500 MPa, 0 MPa, and $+250$ MPa. The test result for $\sigma_{\mathrm{a}} = -250$ MPa is used for validating the predictive abilities of the crack initiation models.

5.2. Optimization results

Two values for the material parameter J, (0.2 and 0.3) have been considered, which are common values in literature for pearlitic steel, see e.g [12, 16, 17]. Table 2 and 3 show the material parameters from literature and the values we obtained for FP_0, m, C_0, and ϵ_c respectively. The identified parameter values are significantly different from those found in the literature.

It should be mentioned that the J-S criterion has been proposed for low cycle fatigue tests, in which the amount of plastic deformation in each loading cycle is small, resulting in large number of cycles to failure [18]. Conversely, in the predeformation tests that we use in this paper [3], the specimens have been subjected to large biaxial strains in each cycle according to Fig. 4a. This results in few number of cycles to failure (very low cycle fatigue). Thus, the material parameters are tuned such that the model predicts large values of damage in each cycle.

Regarding the Kapoor criterion, it is difficult to obtain a good agreement between experimental and simulation results, since the criterion uses less stress-strain information, including only one material parameter. More discussions about these models are presented in the following section.

Table 2: *Material parameters from literature for different crack initiation criteria*

Model	FP_0 [MPa]	m	C_0 [MPa]	ϵ_c
J-S ($J = 0.2$) [17], [16]	0.50	2.00	1224.74	-
J-S ($J = 0.3$) [18], [16]	0.50	2.50	295.42	-
Kapoor [19]	-	-	-	11.5

Table 3: *Optimized material parameters for different crack initiation criteria*

Model	FP_0 [MPa]	m	C_0 [MPa]	ϵ_c
J-S ($J = 0.2$)	29.90	0.41	224.23	-
J-S ($J = 0.3$)	37.90	0.99	47.77	-
Kapoor	-	-	-	0.82

Table 4: *Critical plane direction for $\sigma_a = -500$ MPa at $z = 0.40\,\text{mm}$ and $r = 4.7\,\text{mm}$*

J	[°]	Number of cycles							
		1	2	3	4	5	6	7	8
0.2	θ	80	80	75	30	30	25	25	25
	ϕ	269	269	267	270	270	264	264	264
0.3	θ	80	80	75	70	70	70	65	65
	ϕ	269	269	267	270	270	270	271	271

5.3. Evaluation of crack initiation criteria

In Table 4, the direction of critical plane in each loading cycle for $\sigma_a = -500$ MPa in the integration point at $z = 0.40\,\text{mm}$ and $r = 4.7\,\text{mm}$ (initial position) is shown. Considering $J = 0.3$, the critical plane direction is approximately the same for all cycles. However, for $J = 0.2$, at cycle number 4, there is a sudden change in the direction of the most damaged plane in terms of θ (i.e. the angle between the z-axis and $\boldsymbol{n}$). The contribution of shear loading and normal loading terms in equation (8) is shown in Fig. 6. As it can be seen, for $J = 0.2$, after cycle 3, the shear contribution decreases, while $\Delta\epsilon\,\sigma_{\max}/2$ becomes the dominant term. However, for $J = 0.3$, the shear contribution to FP is dominating in all loading cycles, resulting in the similar trend for FP and $J\,\Delta\gamma\,\Delta\tau$.

Fig. 7 shows the results of life predictions for the J-S crack initiation criterion. In particular, Fig. 7b and Fig. 7d show good agreements between the numerical and experimental results in terms of the number of cycles to failure N_f. Additionally, the fatigue life of the specimen with nominal axial stress of $\sigma_a = -250$ MPa has been predicted very well (especially for $J = 0.3$), which indicates the good predictive ability of J-S criterion. According to Fig. 7c, for the nominal compressive stress of -500 MPa, there is a large fatigue damage growth after cycle 1 and then, damage rate decreases after cycle 3, which is even more significant after cycle 6. From Fig. 5a, it can be seen that stress $\sigma_{z\phi}$ increases after the first cycle. Also, Fig. 5b shows that there is a high shear strain increment from cycle 1 to 3. However, the compressive true stress decreases after the first cycle due to an increase in the diameter of the specimen, and normal strain growth increases. With this in mind, in the case of $J = 0.3$, since shear contribution to FP is larger, the dominant term which controls the damage after cycle 1 is shear loading, resulting in higher damage growth after cycle 1 and before cycle 4. Additionally, due to the fact that, after cycle 4, shear stress as well as strain increment decrease, fatigue damage growth is reduced, particularly towards the last cycles. On the other hand, when the influence of shear strain and stress is lowered by considering a smaller value for J (0.2), the contribution of normal stresses and normal strains increase. With this in mind, although shear stress and strain increment are lowered after cycle 3 (see Fig. 5b), the contribution of normal loading and shear loading terms lead to nearly constant FP (Fig. 6) and in linear damage growth (Fig. 7a).

According to Fig. 8, the Kapoor model does not have

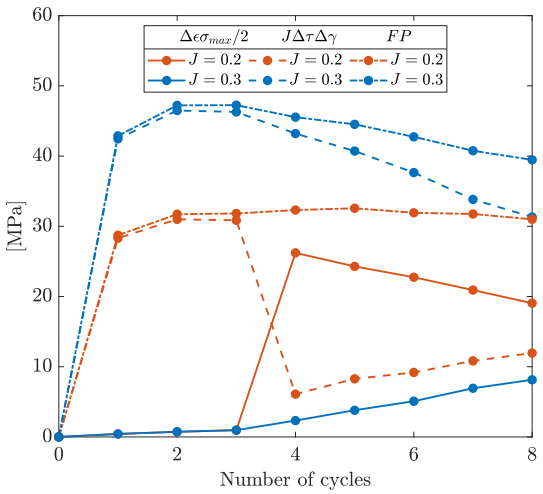

Figure 6: *Contribution of different terms of Fatigue Parameter (FP) for Jiang-Sehitoglu criterion for $\sigma_a = -500$ MPa*

the same ability to give a good agreement between the numerical and experimental results. In most cases, the number of cycles to failure is overpredicted. The reason can partly be the simplicity of this criterion, which makes it difficult to obtain a good fit by using only one material parameter.

It should be mentioned that, the criterion proposed by Jiang-Sehitoglu which considers the summation of fatigue as well as ratchetting damage to be the total damage in each loading cycle (Section 4) has also been evaluated, but no significant improvement compared to J-S criterion was obtained, and the results are thereafter not shown.

None of these criteria account for the evolution of anisotropy, which is known to strongly affect the crack propagation and fracture toughness (see e.g. [1], [2]).

6. Conclusions

Two crack initiation criteria have been evaluated against experimental tests with high shear strains combined with axial loads, similar to the in-field conditions for rails. Finite element simulations with a large strain cyclic plasticity material model have been used to extract stress and strain histories. From the results we can conclude that the Kapoor criterion is not able to predict the number of cycles to failure for these experiments in a satisfactory way. However, the Jiang and Sehitoglu criterion shows a good agreement between numerical and experimental data. For the considered experiments, the identified material parameter values are different from those obtained in standard low cycle fatigue tests on pearlitic rail steel, cf. [18]. From railway mechanics point of view, one advantage with the predeformation tests is that the compressive axial loading and large shear deformations are similar loading conditions to those found in wheel rail contact. Another advantage is that failure initiates in a highly deformed and anisotropic material, which is also often the case in wheel-rail contact conditions. In the experiments considered herein, failure is detected after very few number of cycles (less that 10 cycles) due to large plastic strains that accumulate in each cycle. The number of cycles to failure

in standard low cycle fatigue tests are typically at least 100. To further improve failure predictability for in-field situations, one possible future work is to also include low cycle fatigue experiments [20] in the present evaluation.

While anisotropy develops due to the large shear strain, a good prediction of failure was obtained without considering this. One possible reason can be that the experimental tests in this study did not expose the material to loadings

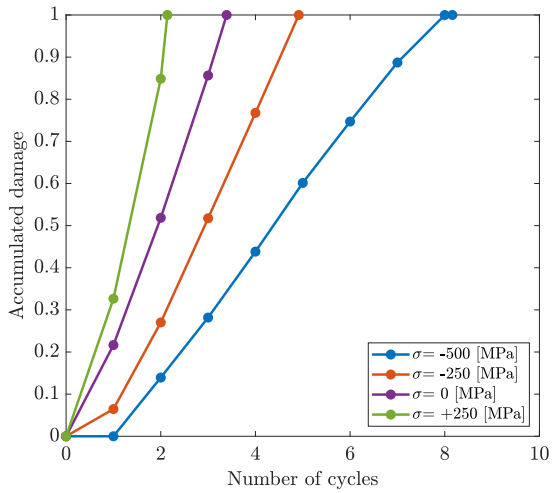

(a) *Accumulated damage (J=0.2)*

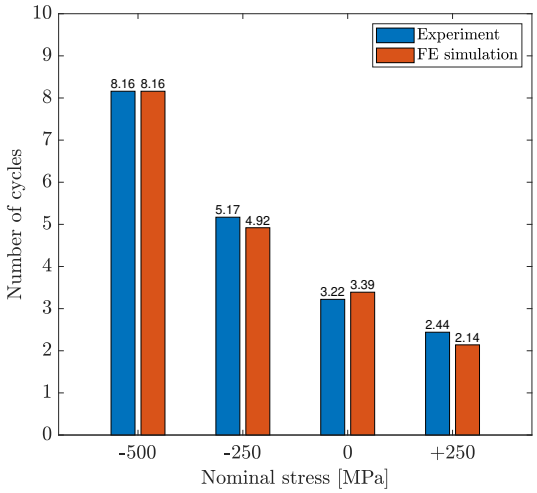

(b) *Number of cycles to failure (J=0.2)*

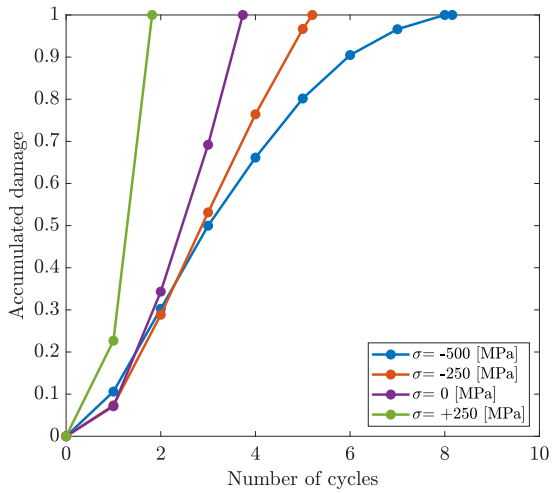

(c) *Accumulated damage (J=0.3)*

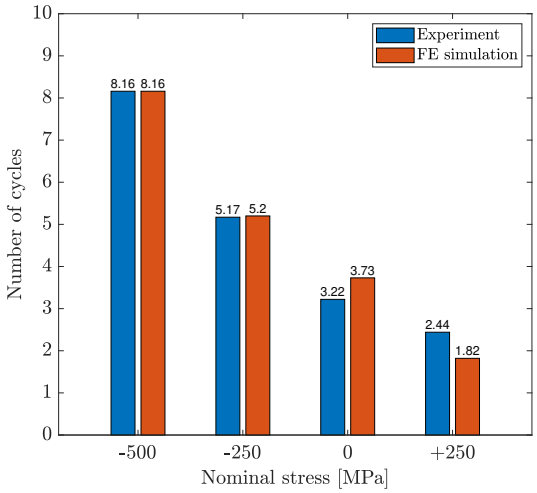

(d) *Number of cycles to failure (J=0.3)*

Figure 7: *Jiang-Sehitoglu crack initiation criterion results*

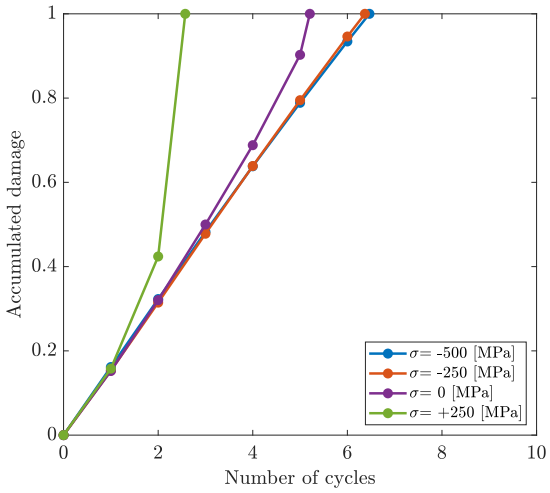

(a) *Accumulated damage*

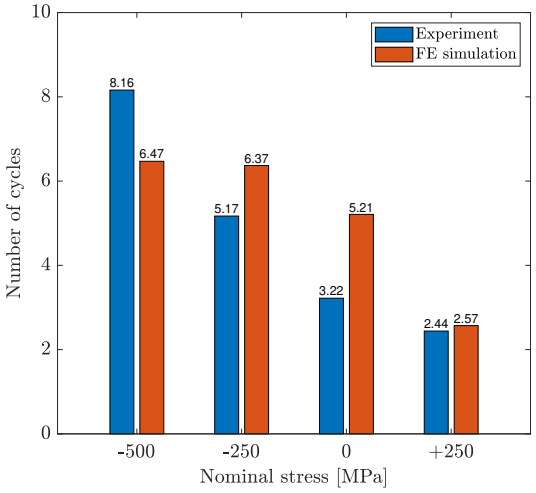

(b) *Number of cycles to failure*

Figure 8: *Kapoor crack initiation criterion results*

where anisotropy becomes important. Another possibility is that the material is not very sensitive to the degree of anisotropy for crack initiation under the investigated conditions. Thus, further experiments should be considered to better understand the interplay between anisotropy and failure.

Acknowledgments
The current study is part of the ongoing activities in CHARMEC – Chalmers Railway Mechanics (www.chalmers.se/charmec). Parts of the study have been funded by the European Union's Horizon 2020 research and innovation program in the project In2Track3 under grant agreements No 101012456. The simulations were enabled by resources provided by the Swedish National Infrastructure for Computing (SNIC) at Chalmers Centre for Computational Science and Engineering (C3SE) partially funded by the Swedish Research Council through grant agreement no. 2018-05973.

References

[1] F. Wetscher, R. Stock, and R. Pippan, "*Changes in the mechanical properties of a pearlitic steel due to large shear deformation*," Materials Science and Engineering A, vol. 445-446, 237–243, 2007.

[2] A. Hohenwarter, A. Taylor, R. Stock, and R. Pippan, "*Effect of large shear deformations on the fracture behavior of a fully pearlitic steel*," in *Metallurgical and Materials Transactions A: Physical Metallurgy and Materials Science*, vol. 42, 2011, 1609–1618.

[3] K. A. Meyer, D. Nikas, and J. Ahlström, "*Microstructure and mechanical properties of the running band in a pearlitic rail steel: Comparison between biaxially deformed steel and field samples*," Wear, vol. 396-397, no. November 2017, 12–21, 2018.

[4] F. Sadeghi, B. Jalalahmadi, T. S. Slack, N. Raje, and N. K. Arakere, "*A review of rolling contact fatigue*," Journal of Tribology, vol. 131, no. 4, 1–15, 2009.

[5] A. Kapoor, "*A re-evaluation of the life to rupture of ductile metals by cyclic plastic strain*," Fatigue Fracture of Engineering Materials Structures, vol. 17, no. 2, 201–219, 1994.

[6] K. Dang Van, M. H. Maitournam, Z. Moumni, and F. Roger, "*A comprehensive approach for modeling fatigue and fracture of rails*," Engineering Fracture Mechanics, vol. 76, no. 17, 2626–2636, 2009.

[7] Y. Jiang and H. Sehitoglu, "*A model for rolling contact failure*," Wear, vol. 224, no. 1, 38–49, jan 1999.

[8] E. S. Alley and R. W. Neu, "*Microstructure-sensitive modeling of rolling contact fatigue*," International Journal of Fatigue, vol. 32, no. 5, 841–850, 2010.

[9] G. Trummer, C. Marte, P. Dietmaier, C. Sommitsch, and K. Six, "*Modeling surface rolling contact fatigue crack initiation taking severe plastic shear deformation into account*," Wear, vol. 352-353, 136–145, 2016.

[10] K. A. Meyer, M. Ekh, and J. Ahlström, "*Modeling of kinematic hardening at large biaxial deformations in pearlitic rail steel*," International Journal of Solids and Structures, vol. 130-131, 122–132, 2018.

[11] K. A. Meyer, M. Ekh, and J. Ahlstrom, "*Anisotropic yield surfaces after large shear deformations in pearlitic steel*," European Journal of Mechanics, A/Solids, vol. 82, jul 2020.

[12] J. W. Ringsberg, "*Life prediction of rolling contact fatigue crack initiation*," 575–586, 2001. [Online]. Available: www.elsevier.com/locate/ijfatigue

[13] D. Systèmes, "*Abaqus*," 2020. [Online]. Available: http://help.3ds.com/

[14] K. A. Meyer, "*Material models*," 2022. [Online]. Available: github.com/KnutAM/MaterialModels

[15] J. A. Nelder and R. Mead, "*A Simplex Method for Function Minimization*," The Computer Journal, vol. 7, no. 4, 308–313, 01 1965.

[16] M. Ghodrati, M. Ahmadian, and R. Mirzaeifar, "*Modeling of rolling contact fatigue in rails at the microstructural level*," Wear, vol. 406-407, 205–217, 7 2018.

[17] E. Kabo, A. Ekberg, P. T. Torstensson, and T. Vernersson, "*Rolling contact fatigue prediction for rails and comparisons with test rig results*," Proceedings of the Institution of Mechanical Engineers, Part F: Journal of Rail and Rapid Transit, vol. 224, 303–317, 1 2010.

[18] O. Onal, D. Canadinc, H. Sehitoglu, K. Verzal, and Y. Jiang, "*Investigation of rolling contact crack initiation in bainitic and pearlitic rail steels*," Fatigue and Fracture of Engineering Materials and Structures, vol. 35, 985–997, 2012.

[19] D. I. Fletcher, F. J. Franklin, and A. Kapoor, "*Image analysis to reveal crack development using a computer simulation of wear and rolling contact fatigue*," Fatigue and Fracture of Engineering Materials and Structures, vol. 26, no. 10, 957–967, 2003.

[20] J. Ahlström and B. Karlsson, "*Fatigue behaviour of rail steel—a comparison between strain and stress controlled loading*," Wear, vol. 258, no. 7-8, 1187–1193, mar 2005.